

Targeting senescent cells by dasatinib and quercetin ameliorates postmenopausal osteoporosis and rejuvenates bone regeneration.

Ying Wang

East China University of Science and Technology

LinBin Che

Shanghai Jiaotong University School of Medicine

Xi Chen

East China University of Science and Technology

Zirui He

East China University of Science and Technology

Dianwen Song

Shanghai Jiaotong University School of Medicine

Yuan Yuan

East China University of Science and Technology

Changsheng Liu (✉ liucs@ecust.edu.cn)

East China University of Science and Technology

Article

Keywords:

Posted Date: April 6th, 2022

DOI: <https://doi.org/10.21203/rs.3.rs-1444778/v1>

License: © ⓘ This work is licensed under a Creative Commons Attribution 4.0 International License.

[Read Full License](#)

Abstract

Clinical therapies developed for estrogen-deficiency-driven postmenopausal osteoporosis (PMO) and related diseases, such as bone degeneration, show multiple adverse effects nowadays. Targeting senescent cells (SnCs) and the consequent senescence-associated secretory phenotype (SASP) with a combination of dasatinib and quercetin (DQ) is a recently developed novel therapy for multiple age-related diseases. Herein, we found that estrogen deficiency induced-bone loss was attributed to a pro-inflammatory microenvironment with SASP secretions and accelerated SnC accumulation, especially senescent mesenchymal stem cells (MSCs) characterized by exhaustion and dysfunction in middle aged rats. Systematically targeting SnCs with DQ strikingly ameliorated PMO and restored MSC function. Local administration of DQ and BMP2 in combination promoted osteogenic differentiation of MSCs and rejuvenated osteoporotic bone regeneration. Our results repurposed DQ as an attractive therapy for treating PMO and related diseases.

Introduction

Osteoporosis (OP), one of the most prevalent chronic diseases among elderly individuals, manifests with notably higher morbidity and a much higher risk of associated bone fracture in postmenopausal women¹⁻³. Estrogen deficiency is now undoubtedly considered the main contributor to imbalanced bone metabolism, especially excess bone resorption which leads to bone fragility in women with PMO, catalogued as type OP⁴⁻⁶. Based on this pathogenesis, current clinical therapies for PMO, including estrogen mediation and bone metabolism regulation, however, have shown multiple adverse effects, as revealed through accumulated evidence⁷⁻⁹. For example, estrogen supplementation, a menopausal hormone therapy, is recommended in the clinic only with precaution because it increases the risk of blood clots formations, as well as breast and uterus cancer development^{10,11}. Bone metabolism regulators, such as bisphosphate and parathyroid hormone (PTH), are also limited due to increased possibility of atypical femoral fracture (AFF) and hypercalcemia¹²⁻¹⁴. Therefore, new therapies for PMO and related diseases are still in urgent demand, particularly those that show few side effects in untargeted tissues.

Senescent cells (SnCs) are characterized by permanent cell cycle arrest, combined with autonomous non-cellular activities, as exemplified by the secretion of inflammatory cytokines, chemokines, and proteases, together termed the senescence-associated secretory phenotype (SASP)¹⁵, which drives the senescence of neighboring normal cells through paracrine signaling^{16,17}. SnCs are proved as culprits of most age-related diseases¹⁷⁻²², and by creating a pro-inflammatory microenvironment, a chronic SASP is also a plausible driver of tissue impairment and degeneration²³⁻²⁵. Notably, recent studies have revealed that estrogen deficiency exacerbated cellular senescence-associated deterioration, such as reactive oxidative stress (ROS) accumulation²⁶, decreased expression of Sirt1²⁷ and decreased telomerase activity²⁸. Cognizant of these results, we hypothesized that PMO may possibly be attributed to SnCs.

The combination of dasatinib and quercetin (DQ), defined as a first generation of senolytic treatment, has been proven to selectively target SnCs and attenuate SASP in multiple tissues^{22,29,30} since first reported in 2015³¹. DQ is now demonstrated to be therapeutic for many aged-related diseases, such as type 2 diabetes³², intervertebral disc degeneration³⁰, atherosclerosis³³, and senile osteoporosis which is classified as type OP²², and it has also shown promising results in clinical trials of diabetic kidney disease³⁴ and idiopathic lung fibrosis³⁵. Considering the plausible relationship between SnCs and PMO, DQ may also perform a positive therapeutic effect in the context of PMO. However, to date, the efficacy of DQ treatment to attenuated PMO is still rarely investigated.

In this study, we thoroughly studied the therapeutic effect of DQ on PMO and related disease. Accelerated SnC accumulation, which contributed to severe bone loss and impaired bone regeneration, was observed in bone tissues of PMO, especially senescent MSCs, as characterized by exhaustion and dysfunction. Targeting SnCs by DQ improved the bone tissue microenvironment, including decreased number of SnCs, attenuation of SASP, and the function restored MSCs. Moreover, systematic treatment with DQ effectively prevented bone loss in PMO models, while local combinatorial treatment with DQ and bone morphogenetic protein 2 (BMP2), an osteo-inductive agent, rejuvenated osteoporotic bone regeneration. Our findings demonstrated that DQ ameliorated PMO and promoted bone repair by creating a pro-regenerative microenvironment, and repurposed the senile OP (type) -indicated drug DQ as an attractive therapy for treating PMO (type) and related diseases.

Results

Systematic treatment with the senolytic drug DQ prevented bone loss in middle-aged postmenopausal osteoporotic rats (PMO rats)

We first sought to determine whether the senolytic drug DQ, which has been in clinical trials for many age-related diseases, could alleviate PMO systematically^{36,37}. Considering that most postmenopausal women are in middle age, we chose 12-month-old (12-mo) female rats as the animal model to match the pathological age to the maximum extent. The middle-aged rats were subjected to a sham operation (M-SHAM), or ovariectomy with (M-DQ) or without (M-OVX) DQ treatment afterwards, and the femurs were dissected at the 16th month after surgery for analysis (Fig. 1a). Systematic DQ treatment significantly increased the enrichment and density of trabecular bone in the M-DQ group compared to that in the M-OVX group (Fig. 1b). To investigate the trabecular bone microarchitecture, areas in the distal femur were further analyzed. The 3D obtained micro-computed tomography (μ CT) images demonstrated that DQ treatment substantially resulted in better femur trabecular bone microarchitecture (Fig. 1c), with elevated bone volume fraction (BV/TV, Fig. 1d) and trabecular number (Tb.N, Fig. 1e) by approximately 2 fold, as well as the declined trabecular separation (Tb.Sp, Fig. 1f) and structure model index (SMI, Fig. 1g). Consistent with these results, increased trabecular number and growth plate amelioration were also observed in the DQ-treated postmenopausal osteoporotic rats (PMO rats) (Fig. 1h). In addition, the possible side effects of DQ on other organs were examined (**Fig S1**). Significant tissue damage or

pharmacological toxicity was not observed in the kidney, lung, spleen, liver and heart tissues, suggesting the combination of DQ could be a favorable candidate for PMO treatment. In summary, these results demonstrated that, for the first time to our knowledge, systematic treatment with the senolytic drug DQ ameliorated PMO in middle-aged rats.

Accumulation of SnCs accelerated bone loss in middle-aged PMO rats

We next investigated whether PMO was related to SnCs in bone tissues. SnCs, which appear throughout the lifespan, are suspected to be cleared by the immune system at a young age but accumulate rapidly in old age, probably due to the decreased clearance capacity of the aged immune system^{38,39}. Although a steep increasing number of senescent cells in bone tissue was accounted in individuals of senile OP (type 2)²², whether SnCs were accumulated during PMO (type 1) was unclear. A previous study has reported that SnCs were not remarkably accumulated in the bone tissue of young OVX mice, and found that eliminating SnCs did not rescue the bone loss⁴⁰. However, our results showed a therapeutic effect of DQ treatment in middle-aged rats, indicating a probable accelerated SnC accumulation in middle-aged PMO rats. Hence, to thoroughly reveal the relationship between SnCs and PMO, both 6-mo (young, Y) and 12-mo (middle-aged, M) rats were subjected to a sham operation (Y-SHAM or M-SHAM) or ovariectomy (Y-OVX or M-OVX), with 19-mo (old, O-SHAM) rats as naturally aged control for comparison analysis (**Fig. 2a**). Deteriorated skeletal architecture and remodeling were observed in the OVX groups compared with SHAM groups at both young and middle age stages (**Fig. 2b**)- including reduced BV/TV (**Fig. 2c**) and Tb.N (**Fig. 2d**), as well as increased Tb.Sp (**Fig. 2e**) and SMI (**Fig. 2f**). Notably, the Tb.Sp of the M-OVX rats was significantly higher (3-fold) than that of the Y-OVX rats, but was equivalent to that of the O-SHAM rats (**Fig. 2e**), indicating the deterioration of microenvironment in the M-OVX rats. Although the BV/TV and Tb.N of the M-OVX rats and Y-OVX rats showed no significant differences, consistent with observations reported in a previous study⁴¹, the more significant value reduction was observed in middle-aged OVX rats (**Fig. 2c-d**). Furthermore, a more serious destruction of trabecular bone structure was observed in hemoxylin and eosin (H&E) stained images (**Fig. 2g**), simultaneously with a decreased number and more structural disorders in trabecular bone, similar to O-SHAM rats. These results showed that middle-aged PMO rats exhibited more severe bone structure deterioration equivalent to that of naturally aged rats.

To examine whether SnCs contribute to PMO, p16 (also known as cyclin-dependent kinase inhibitor 2a and highly expressed in SnCs) and p53 (another typical biomarker of SnCs) levels were measured to identify SnCs in bone tissue. A remarkable accumulation of both p16 and p53 positive SnCs was observed in the M-OVX rats compared with that in the Y-OVX rats and was equivalent to that in the O-SHAM rats (**Fig. 2g-k**). In summary, we suggest that SnC accumulation accelerated bone loss in middle-aged PMO rats, and established correlation of the pathogenesis of type 1 and type 2 osteoporosis.

DQ eliminated SnCs in middle-aged PMO rats

Considering that SnCs accumulated in middle-aged PMO rats, we next investigated the effect of DQ on SnCs in PMO rats at different age stages. Both Y-OVX and M-OVX rats were administrated DQ orally for two months (Y-DQ and M-DQ) and then the lumbar vertebrae were dissected for analysis. Treatment with DQ reduced the SnC number in the M-DQ rats compared with the M-OVX rats, with the decreased expression of p16 and p53 by approximately twofold. However, no significant difference was observed among young rats (**Fig. 3a, b**). Consistent with the lumbar vertebrae results, DQ reduced the number of p16-positive and p53-positive SnCs in the femur, nearly a twofold reduction compared with that in the M-OVX group (**Fig. 3c-f**). Our results showed that SnCs accumulated in middle-aged PMO rats, as characterized by increased expression of p16 and p53, and DQ effectively eliminated SnCs, as indicated by decreased p16 and p53 expression in middle-aged PMO rats.

MSCs exhibited senescence-associated characteristics in middle-aged PMO rats

Stem cells, especially MSCs, are key contributors to bone formation and regeneration due to their excellent self-renewal and osteogenic capacities. However, MSC senescence, characterized by exhaustion and inappropriate adipogenesis, is induced by the pro-inflammatory microenvironment during aging, and is considered the culprit of osteoporosis and degeneration^{21,42-44}. To further probe the performance of MSCs in middle-aged PMO rats, we first examined the frequency and self-renewal capacity of the MSCs. Femurs and tibias from middle-aged SHAM or OVX group rats were dissected, and cells were isolated for flow cytometry analysis and colony-forming unit (CFU) assay (**Fig. 4a**). CD45-negative, CD44-positive and CD29-positive cells were identified as MSCs. The frequency of MSCs in OVX group rats decreased by 4.9% compared with that in the SHAM group rats (**Fig. 4b-d**). Consistent with the flow cytometry results, the CFU assay showed a decreased self-renewal capacity, by approximately fivefold, in the OVX group (**Fig. 4e**). The exhaustion of MSCs strongly suggested MSC senescence in middle-aged PMO rats.

Based on aforementioned findings, the relationship between MSC exhaustion and senescence was further investigated through a transcriptome analysis. We hypothesized that MSC behavior was regulated by estrogen-deficiency induced microenvironment. To mimic the microenvironment *in vitro*, serum extracted from OVX rats were mixed with cell culture medium to prepare the conditioned medium (CM). Normal MSCs (isolated from one-month-old rats) were exposed for 3 days to CM containing serum from M-SHAM (SHAM CM), M-OVX (OVX CM) and O-SHAM (Old CM) rats for 3 days, and the transcriptome of the different CM-treated MSCs was analyzed by RNA sequencing. The transcriptomic profiles of each group clustered distinctly, as demonstrated by principal component analysis (PCA, **Fig. S2a**), and the differentially expressed genes (DEGs) between the SHAM and OVX groups were defined with a cutoff of adjusted p value < 0.05 and $|\log \text{fold change}| \geq 1$ (**Fig. S2b**). The DEGs downregulated in the OVX group were enriched in the cell cycle, DNA repair (homologous recombination, Fanconi anemia pathway, mismatch repair and base excision repair), and DNA replication pathways (**Fig. 4f**), which all have been correlated with cellular senescence. Common DEGs identified in both OVX vs. SHAM and Old vs. SHAM analyses accounted for 22.8% of total DEGs identified and were hierarchically clustered following the same trend in the OVX and Old groups compared with that in the SHAM group (**Fig. 4g, h**), in which DEGs were also enriched in pathways similar to those identified in OVX vs. SHAM analysis (**Fig. 4i**). Gene-set

enrichment analysis (GSEA) showed similar regulatory effects between MSCs in the OVX and Old groups, with downregulation of cell cycle pathway and upregulation of steroid biosynthesis pathway (**Fig. 4j**). To determine whether the features of MSC exhaustion in middle-aged PMO rats were similar to those of senescent MSC exhaustion, we further investigated the cell cycle pathway. MSCs in OVX group exhibited G1/S downregulation which was also observed in senescent MSCs, with lower levels of cyclin E (CycE), cyclin A (CycA), cell division cycle 6 (Cdc6), cell division cycle 45 (Cdc45), and minichromosome maintenance complex component 5 (MCM5) (**Fig. 4k**). These results demonstrated that MSCs in the middle-aged PMO rats exhibited senescence-associated hallmarks and presented transcriptomic profiles similar to that of senescent MSCs in CM containing old rat serum.

DQ rescued MSC exhaustion and restored MSC function via attenuating SASP

To further investigate the effect of DQ treatment on the MSC fate, we evaluated the cellular senescence, proliferation and osteogenesis capability of MSCs after treatment with CM composed of serum extracted from M-DQ rats (DQ CM). First, MSC senescence was delayed by DQ as proven by decreased senescence-associated β -galactosidase (SA- β -gal) positive cell numbers (**Fig. 5a**) and lower gene expression of p16, p21 and p53 in the DQ CM group (**Fig. 5b**). To account for possible cell cycle arrest, we conducted the cell cycle test by performing flow cytometry, and the results showed a decreased percentage of cells in the DQ CM group in the G1 phase compared with that in the OVX CM group, suggesting reestablished cell cycle progression after DQ treatment, not arrest in the G1 phase (**Fig. 5c, d**). Furthermore, the expression of SASP genes was strikingly downregulated by DQ; in contrast, these genes were highly expressed in OVX CM group, indicating that DQ attenuated the development of a pro-inflammatory microenvironment in the PMO context (**Fig. 5e**). MSC exhaustion was also rescued by DQ, demonstrated by an increased number of colonies (**Fig. 5f, g**) and increased proliferative ability (**Fig. 5h**). In addition, DQ improved MSC morphology, showing diminished lipofuscin formation (**Fig. S3**). To further investigate the effect of DQ on MSCs in PMO rats, Alizarin red S (ARS) staining was performed. The results showed that the impaired osteogenesis ability of the MSCs in OVX CM, characterized by decreased calcium nodules, was significantly restored by DQ (**Fig. 5i**).

Transcriptomes of the MSCs in SHAM CM, OVX CM, or DQ CM were compared by RNA sequencing to determine the regulation of senescence-associated processes in the PMO context after treatment with DQ. The transcriptomic profiles of the DQ group showed distinct clusters (**Fig. S2a**), and the DEGs between the OVX and DQ groups were identified on the basis of a cutoff adjusted p value < 0.05 (**Fig. S2c**). Compared with the effect on the MSCs in OVX CM, DQ upregulated pathways related to DNA replication, DNA repair and cellular senescence; the DEGs in these pathways were found to be significantly downregulated in the OVX vs. SHAM group analysis (**Fig. 6a**). Common DEGs identified in both the DQ vs. OVX and DQ vs. SHAM analyses accounted for 31.5% of the total DEGs, showing the same trend in the DQ and SHAM groups, and these DEGs were enriched in some of the same pathways identified in the OVX vs. SHAM analysis (**Fig. 6b-d**). The GSEA showed the upregulation of the cell cycle-related genes and downregulation of steroid biosynthesis-related genes in DQ-treated MSCs, in contrast to the findings in the Old or OVX MSCs (**Fig. 6e**). In addition, DQ also upregulated homologous

recombination and glutathione metabolism pathways (**Fig. S2d**), which contribute to anti-senescence effects. These results demonstrated shifted transcriptome profiles of MSCs in OVX CM toward a profile similar to that of SHAM MSCs after DQ treatment (**Fig. 6b-e**). The ten most active hub genes in the MSCs in DQ vs. OVX analysis were predicted using Cytoscape software (**Fig. 6f, Table S1**). Interestingly, these genes all intersected in the OVX vs. SHAM, Old vs. SHAM and DQ vs. OVX analysis (**Fig. 6g**) and were all downregulated in the OVX and Old groups but upregulated in the DQ group (**Fig. 6h**), indicating that DQ mainly regulated senescence-associated processes in PMO. In summary, DQ regulated a transcriptome shift toward the SHAM phenotype, rescued MSC exhaustion and restored MSC function by attenuating the SASP.

Local implantation of DQ-encapsulated and BMP2-fixed hydrogel rejuvenated bone regeneration

The aforementioned findings demonstrated that DQ effectively ameliorated PMO in a systematic way, but notably, PMO leads to many complications with serious consequences, for which DQ may also exert a positive effect. Local osteoporotic fracture is a typical complication, and the risk in women is as high as 40%, making it a major cause of death, disability, and worldwide healthcare costs⁴⁵. Here, we investigated the effect of DQ on bone regeneration in a PMO defect model through the combination and local administration of DQ and human recombinant bone morphogenetic protein 2 (BMP2), a commonly used osteo-inductive agent. To improve the microenvironment for local bone defect regeneration, DQ was expected to be released prior to BMP2, resulting in a negatable influence of the SASP. Therefore, we fabricated a DQ-encapsulated and BMP2-fixed injectable hydrogel for implantation (DQ+BMP2) (**Fig. 7a**). To realize sequential administration of DQ and BMP2 locally *in vivo*, bioglass microspheres with mesopores (MBG) of 8 nm, which was compatible with the BMP2 size (7.5 nm), were fabricated as previously described for sustained release of BMP2⁴⁶ (**Fig. S4a, b**). DQ was directly mixed into the gelatinous methacryloyl (GelMA) hydrogel and was released earlier than BMP2 (**Fig. S4c**). The encapsulated amount of D and Q were 685 $\mu\text{g mL}^{-1}$ and 68.5 $\mu\text{g mL}^{-1}$, respectively. The micro-CT analysis demonstrated that local treatment with DQ had a synergistic effect with BMP2 on bone regeneration, as proven by significantly increased newly formed bone, especially cortical bone, in the DQ+BMP2 group (**Fig. 7b**). Compared with the effect of BMP2 released separately, DQ elevated the BV/TV (**Fig. 7c**), Tb.Th (**Fig. 7d**) and Tb.N (**Fig. 7e**) by approximately twofold and decreased the Tb.Sp (**Fig. 7f**) in the DQ+BMP2 group. Consistent with these results, the H&E- and Masson-stained images showed orderly arranged trabeculae accompanied by abundant infiltration of bone marrow cells in the cavities (**Fig. 7g, S5a, S5b**). Less cell infiltration was observed between bone trabeculae in the BMP2 group.

Next, we investigated the mechanism creating of BMP2 and DQ synergism in bone regeneration by dissolving DQ into OVX CM. The concentration of DQ for inducing MSC senescence was tested using an oxidative stress-induced senescence model (**Fig. S6a**). The optimal concentrations of DQ in combination with quercetin (Q10) was 10 μM , and it was 10 nM with dasatinib (D10) (**Fig. S6b-e**). Senescent MSCs (Sen) were selectively eliminated, while proliferating non-senescent MSCs (Pro) survived. After 3 days of DQ-treatment, MSCs (DQ) exhibited decreased proliferation by approximately 27% compared to Sen MSCs due to the clearance. However, when DQ was removed on the 4th day, the MSCs restored the

proliferation capability and increased approximately 23% viability compared to that under the treatment of DQ, throughout the following three days (**Fig. S6e**). In a Transwell experiment, decreased p16, p21, p53 and SASP expression was found in proliferating MSCs cocultured with DQ MSCs (**Fig. S6g**).

To investigate the synergistic effect of DQ and BMP2, MSCs were sequentially treated with conditioned medium (SHAM, OVX, or DQ CM) for 7 days and complete medium containing a low dose of BMP2 (SHAM+BMP2, OVX+BMP2, or DQ+BMP2) for another 7 days (**Fig. 7h**). p16 expression on the 7th day was downregulated by local administration of DQ, while both pSmad1/5/9 (a signal transduction molecule involved in BMP2 pathway activation) and col expression was upregulated (**Fig. 7i-k**). ARS and Oil red O staining on the 14th day revealed that compared with MSCs in OVX+BMP2 CM, MSCs in DQ+BMP2 CM showed restored osteogenic differentiation and decreased adipogenic differentiation, which may have led to bone loss as reported elsewhere^{43,47} (**Fig. 7l, m**). However, when treated of DQ and BMP2 simultaneously (DQ/BMP2), senescent MSCs exhibited inferior osteogenesis compared with that treated with BMP2 only (**Fig. S7**). We proposed that the improved osteogenesis after sequential treatment with DQ and BMP2 (DQ+BMP2) might be attributed to the improved microenvironment and recovered proliferating ability, while the inferior osteogenesis after the simultaneous treatment of DQ and BMP2 (DQ/BMP2) was ascribed to the decreased amount of MSCs (**Fig. S6e**). These results solidified our design of the hydrogel with sequential releasing of DQ to regulate the microenvironment and followed by BMP2 to induce higher osteogenesis. The *in vivo* immunofluorescence staining analysis further confirmed the increase in osteogenesis, by revealing higher expression of Runt-related transcription factor 2 (Runx2, **Fig. 7n, S8a**), decreased expression of p16 and p53 (**Fig. 7o-p, S8b-c**) and diminished matrix metalloproteinase 9 (MMP9, a typical protease in the SASP, **Fig. 7q, S8d**). Taken together, local administration of DQ combined with BMP2 showed a synergistic effect on bone regeneration by inhibiting cellular senescence and promoting pSmad1/5/9 pathway activation.

Discussion

Inadequate pathogenesis investigation has been an intractable problem in PMO therapy development. Up to date, although estrogen deficiency is considered a main contributor to PMO^{4,5,48} and may potentially be related to SnCs²⁶⁻²⁸, the interaction and extent of these three factors at different age stages have rarely been reported. In this study, we showed that exacerbation of bone loss equivalent to that of naturally aging rats was induced by estrogen deficiency in middle-aged rats but not in young rats (**Fig. 2b, g**), suggesting that middle-aged animals may be the priority for PMO studies. Furthermore, our results indicated that in the middle-aged rats, PMO was attributed to the deterioration of the bone microenvironment, which manifested as SnC accumulation, MSC senescence and increased secretion of SASP factors (**Fig. 5e, 7q**). Consistent with bone loss, SnCs accumulated in middle-aged aged rats but not in young rats (**Fig. 2h, j**). A previous study²⁶ showed that SnCs did not accumulate in the bone tissue of young OVX mice, but our findings proved that SnCs accumulated in an age-dependent way as a complement. Additionally, gradual SnC accumulation over 12 months and 18 months has been reported elsewhere²², but our results showed a steep increase in SnCs after 12 months in PMO rats, demonstrating

that estrogen deficiency accelerated SnC accumulation in middle-aged rats. Although several studies have established the relationship between estrogen deficiency and osteoblast⁴⁹ and/or osteocyte⁵⁰ senescence, MSCs, which serve as the parental pool for osteoblasts and chondrocytes, are more critical than differentiated cells for bone remodeling. In this study, we found that estrogen deficiency accelerated MSC senescence and thus caused decreased bone formation in middle-aged rats (Fig. 8). RNA sequencing revealed that the transcriptomic profiles of MSCs in PMO rats shifted toward that of naturally senescent MSCs, which were mainly characterized by the downregulation of cell cycle genes (Fig. 4b-e). PMO (type) and senile (type) osteoporosis are recognized as two distinct categories of involuntional osteoporosis⁴. While the early PMO is considered to be caused by estrogen deficiency and excess bone resorption, senile osteoporosis is attributed to aging process such as cellular senescence and inadequate bone formation. Our results revealed that regulation of SnCs and senescent MSCs might enhance PMO therapies, and provided new insights into the discriminated pathogenesis of PMO and senile osteoporosis⁴⁸.

Furthermore, for the first time, we found that systematic administration of DQ showed excellent performance in treating PMO (Fig. 1, Fig. 8). DQ diminished the number of SnCs in bone tissue and rescued MSC senescence by attenuating the SASP (Fig. 5a), which led to reestablished cell cycle progression (Fig. 5d) and recovered MSC proliferative ability (Fig. 5f). In particular, DQ promoted osteogenesis of MSCs in PMO rats (Fig. 5i) and contributed to increased bone formation. Besides, DQ attenuated the upregulation of age-associated pathways, predominantly through the 10 hub genes (Fig. 6f, Fig. 6g, **Table S1**) related to DNA replication and led to a transcriptome profile shift that caused the MSCs in PMO rats to resemble non-senescent MSCs (Fig. 6c-e). Finally, we demonstrated that local administration of DQ with a sequential combination of BMP2 had a synergistic effect on bone regeneration (**Fig. 7eb, g**, Fig. 8), providing insights into therapies for PMO-related local bone fractures. Our research is one of few investigations locally targeting SnCs only in specific tissues^{21,51}. Our *in vivo* results showed that DQ eliminated SnCs locally in the defect area (Fig. 7o, p), and *in vitro* observations revealed that DQ promoted osteogenic differentiation of MSCs by activating the pSmad1/5/9 pathway (Fig. 7j).

In conclusion, we proposed, for the first time, that the senolytic drug DQ ameliorated PMO and related diseases, as proved by systematically preventing bone loss and locally rejuvenating bone regeneration, in synergy with BMP2. Mechanistically, DQ improved the bone microenvironment, with decreased SnC accumulation, rescued MSC exhaustion and recovered MSC function. Our findings provide insights into the complex, multifactorial mechanisms that underlie PMO and repurposed the senile OP-indicated drug DQ as an attractive novel therapy for treating PMO and related diseases..

Materials And Methods

Animals

The Animal Care and Use Committee of the School of Medicine of Shanghai Jiao Tong University approved all experimental animal procedures and animal care (License number: 20180901). Female rats of different ages were assigned to three groups: young (6-mo to 8-mo, Y), middle (12-mo to 14-mo, M) and old (19-mo to 21-mo, O) groups. To investigate whether PMO can be attributed to SnCs, young, middle-aged and old female rats were randomized and received either a sham operation (SHAM, Y-SHAM or M-SHAM) or were ovariectomized (OVX, Y-OVX or M-OVX), with some in the latter group treated with DQ (Y-DQ or M-DQ) (n = 6). All rats were euthanized at after 2 months, and lumbar or femurs were dissected for senescent associated analysis. Furthermore, old female SHAM (O-SHAM) rats served as natural aging models in the assessments (n = 6). D and Q were diluted in 10% PEG400 (diluted in DI water) and administrated every two weeks by oral gavage at dosages of 5 mg kg⁻¹ and 50 mg kg⁻¹, following methods previously reported²².

Micro-CT analysis

Femurs were dissected from Y-SHAM or Y-OVX, M-SHAM or M-OVX, and O-SHAM rats for micro-CT analysis. A micro computed tomography instrument (Bruker Optik GmbH, Belgium) was used to evaluate the in vivo bone regeneration of the models. Skull, femur and lumbar vertebra were harvested and fixed in 4% paraformaldehyde 36 h before micro-CT scanning. Samples were scanned at 18 μm pixel resolution (1 mm aluminum filter, 65 kV, 380 μA). The cranial defect region was visualized in the coronal, sagittal, and transaxial planes with adjacent tissue using Data Viewer software. A cylinder-shaped region of interest (ROI) with a 4 mm diameter corresponding to the defect site was selected. The analysis of the regenerated neo tissue was evaluated with CTAn software, according to factors such as BV, BV/TV, BS, Tb.Th, Tb.N and Tb.Sp. Representative 2D and 3D reconstructed images were acquired and processed with SkyScan Data Viewer and CTVol software, respectively. For the femur, coronal and sagittal planes were visualized, and the region 1.5 mm immediately below the growth plate was analyzed to quantify the trabecular bone volume, the structure model index (SMI) and BV/TV. ROIs of the femur in the 1 mm medial position and the third lumbar vertebra were reconstructed and processed by SkyScan CTVol and CTVOx software, respectively.

Flow cytometry of MSCs

Tibiae and femurs from M-SHAM or M-OVX rats were dissected, cleaned of soft tissue and flushed with staining buffer (10% fetal bovine serum (FBS, Gibco) in PBS). After straining through a 40 μm nylon filter, the cells were washed in staining buffer and pelleted at 800 rpm at 4 °C for flow cytometry preparation. The cell pellet was resuspended in staining buffer with fluorochrome-conjugated antibodies (BioLegend, USA) against CD45 (202225, 1:500), CD29 (102215, 1:200), and CD44 (203906, 1:500). Flow cytometry was performed with a CytoFLEX Platform (Beckman, USA).

Cell culture and conditioned medium generation

MSCs were isolated as previously described⁵² from 1-mo rats. Primary MSCs expanded to passage 3 in growth medium consisting of α-MEM with 10% FBS and 1% penicillin–streptomycin were used in all

comparison experiments. Condition medium (CM) consisted of α -MEM, 0.2% FBS, 15% serum collected from 14-mo sham (SHAM), 14-mo ovariectomized (OVX), or 21-mo sham (Old) rats, and 1% penicillin–streptomycin. To systematically study the effect of DQ, DQ CM was mixed with serum from 14-mo OVX rats orally treated with DQ for 2 months. For investigation into local effects, DQ CM was obtained by directly mixing DQ with OVX CM to mimic the *in vivo* local administration condition.

For studies of systematic effects on osteogenesis and adipogenesis, cells were cultured with 10% FBS, 100 nM dexamethasone, 1 μ M L-ascorbic acid-2-phosphate and 10 ng ml⁻¹ TGF- β 1, maintained for 7 days and stained with a BCIP/NBT alkaline phosphatase color development kit (Beyotime, C3206). For differentiation experiments in the context of local effects, 10,000 MSCs per well were plated in 24-well culture plates with complete medium and then transferred to SHAM, OVX or DQ CM with BMP2 (0.2 μ g mL⁻¹) for 14 days. The optimal concentration of DQ (D10 plus Q10) obtained from the H₂O₂-induced model was dissolved in OVX CM to generate DQ CM. An oxidative stress-induced senescent model was established with 100 μ M H₂O₂ for 2 hours. Cells were analyzed on the 7th day for p16 (a senescent marker), 6 hours after BMP2 treatment for pSmad1/5/9 (necessary for BMP2 pathway activation), and finally on the 14th day for col I (osteogenesis) levels. At the end of the differentiation culture period, cells were stained with ARS (Beyotime, C0148S) or Oil red O (Beyotime, C0158S). To quantify alkaline phosphatase (ALP) activity, 20,000 MSCs per well were plated in 24-well culture plates with complete medium and then transferred to SHAM, OVX or Sim-DQ CM with BMP2 (0.2 μ g mL⁻¹) for 7 days. ALP activity was analyzed by an Alkaline Phosphatase Assay Kit (Beyotime, P0321S) according to the manufacturers' instructions.

Colony-forming unit (CFU) assay

For the colony-forming unit assay of primary cells, single cells flushed from bone marrow were resuspended in α -MEM with 20% FBS (Gibco, Australia) and 1% penicillin–streptomycin (Thermo Fisher, 15140163), and the obtained single cells were plated at a density of 5000 cells cm⁻² for 7 days. MSC colonies were identified, and the number of colonies per plate were counted for each rat. For microenvironment investigation, 100 MSCs in passage 3 were plated and treated with CM for 7 days. The cells were fixed with 70% ethanol and stained with Giemsa staining solution (Beyotime, C0131).

Protein extraction and western blot analysis

To examine senescent markers of bone tissue, lumbar vertebrae (L1 to L5) were used for protein extraction. Briefly, vertebrae were dissected, cleaned of soft tissues, and ground in a liquid nitrogen atmosphere. Then, RIPA lysis buffer containing phenylmethanesulfonyl (1 \times 10⁻³ M) was added to the ground powder for protein extraction. Lysates were separated on 10% SDS–PAGE polyacrylamide gels and transferred to PVDF membranes (0.22 μ m). After being blocked with blocking buffer (Beyotime, China) for 15 min at room temperature, the membranes were incubated with primary antibodies against p16 (Invitrogen, MA5-17142, 1:1000) and p53 (CST, 2524T, 1:1000) overnight at 4 °C and then with

horseradish peroxidase (HRP)-conjugated secondary antibodies (Jackson ImmunoResearch, USA) at room temperature for 1 h.

To investigate the impact of the microenvironment on MSC behavior, cells were cultured in CM for 7 days and CM containing BMP2 ($0.2 \mu\text{g mL}^{-1}$) for another 7 days. Protein was extracted on day 7, day 7 plus 6 h, and day 14 to analyze p16, pSmad1/5/9, and col expression, respectively.

Histological and immunohistochemical evaluation

For evaluation of bone histology, samples were fixed in 4% paraformaldehyde for 48 h and then decalcified in 10% ethylenediamine-tetraacetic acid for 3 weeks before being dehydrated with gradient alcohols and embedded in paraffin, and 5 μm thick contiguous sections were sliced for H&E-, Masson- and IF- staining analysis. For IHC staining, slides were processed for heat-induced epitope retrieval in a microwave oven by heating in 0.01 M citrate buffer for 9 min. The sections were incubated in diluted normal serum for an hour and then incubated with primary antibodies, including antibodies against p16 (dilution 1:120, Abcam) and p53 (dilution 1:120, Abcam), at 4 °C for 24 h. After the sections were rinsed with PBS three times and incubated with a biotinylated secondary antibody (dilution 1:150) for 1 h, immunoreactivity was visualized in a solution of 0.01% H_2O_2 and 0.05% diaminobenzidine, which generated a brown reaction. Nuclei were revealed with hematoxylin staining. All slides were observed with an optical microscopy (Leica, Germany).

RNA sequencing and analysis

Total RNA from MSCs after treatment with SHAM, OVX, DQ and Old CM for 3 days was extracted by TRIzol and purified with poly-T oligo-attached magnetic beads. Then, sequencing libraries were established with an MGIEasy RNA library kit (MGI, China), and samples were subjected to DNBSEQ and mapped to the *Rattus norvegicus* reference genome (GCF_000001895.5_Rnor_6.0, July 2014) using HISAT2 software (v2.0.4). Bowtie2 (v2.2.5) and RSEM software (v1.2.8) were used to identify differentially expressed genes based on the DEseq2 method. All differentially expressed genes (DEGs) were defined with a false discovery rate-adjusted p value less than 0.05 and $|\log \text{fold change}| \geq 1$. Pathways enriched with DEGs were analyzed and visualized based on Kyoto Encyclopedia of Genes and Genomes (KEGG) pathway⁵³ and Pathview⁵⁴ with a p value < 0.05. All aligned genes were imported into GSEA software (MSigDB, v7.3), and the statistically significant gene sets with $|\text{NES}| > 1$, nominal p value < 0.05 and FDR < 0.25 were examined⁵⁵. The ten most active hub genes were predicted by the MCC ranking method and based on the PPI network downloaded from version 11.5 of the STRING database and visualized with Cytoscape software (v3.10.0).

Senescence-associated- β -galactosidase assay

SA- β -gal activity was detected using a senescence β -galactosidase staining kit (CST, 9860S) following the manufacturer's instructions. MSCs were cultured in complete medium or different CMs for 7 days and then washed twice with PBS. Cells were fixed with 4% paraformaldehyde for 15 min and incubated with

SA- β -gal staining solution at 37 °C overnight. For H₂O₂-induced senescence, cells were treated with 100 μ M H₂O₂ for 2 h and later cultured in complete medium until analysis.

Cell cycle analysis

MSCs were cultured in SHAM, OVX and DQ CM for 24 h. Then, the cells were fixed with 70% ethanol for 2 h. Subsequently, the cells were stained with a PI/RNase staining kit (Dojindo, C543) and analyzed by flow cytometry.

Quantitative RT-PCR

After incubation in CM for 3 days, total RNA was extracted using TRIzol (TaKaRa, Japan), and the purity and concentration were quantified by a NanoDrop 2000 (Invitrogen, USA). Reverse transcriptase was performed using an iScript cDNA synthesis kit (Bio-Rad, 1708891). PCRs were performed using iTaq Universal SYBR Green Supermix (Bio-Rad, 1725121) in a CFX96 Real-Time System (Bio-Rad, USA). All experiments were performed in triplicate. The primer sequences used are listed in Table S2.

In vivo bone defect model and scaffold implantation

The sequentially released scaffold consisted of mesoporous bioglass (MBG) microspheres and an injectable 10% GelMA hydrogel. GelMA hydrogel (Control), hydrogel with DQ (DQ), hydrogel with BMP2 (BMP2), and hydrogel with both DQ and BMP2 (DQ+BMP2) were implanted into the defect area. Released quercetin was quantified at an OD value of 376 nm, and BMP2 was detected with a human BMP2 ELISA kit (ENZO-1, ASB-OKEH00025).

Statistical analysis

All data are presented as the means \pm standard deviation. Statistical analysis was assessed using GraphPad Prism 8.0 statistical software. Quantification was determined with ImageJ software. One-way analysis of variance was used to perform statistical analyses, and $p < 0.05$ was considered to be statistically significant; * $p < 0.05$, ** $p < 0.01$, *** $p < 0.001$, **** $p < 0.0001$, ns, not significant.

Declarations

Acknowledgments

Funding:

This work is supported from:

Frontiers Science Center for Materiobiology and Dynamic Chemistry (No. JKVD1211002)

Natural Science Foundation of China for Innovative Research Groups (No.51621002)

Author contributions:

Conceptualization: W.Y. and L.C

Methodology: W.Y.

Investigation: W.Y. and L.C.

Visualization: W.Y.

Supervision: C.L., Y.Y., and D.S.

Writing—original draft: W.Y. and L.C.

Writing—review & editing: W.Y., L.C., C.L., Y.Y. and D.S.

Competing interests: All other authors declare they have no competing interests.

Data and materials availability:

All data are available in the main text or the supplementary materials. The databases used in this study, including KEGG (<https://www.genome.jp/kegg/>), Pathview (<https://pathview.uncc.edu/>), STRING (<https://www.string-db.org/>) and GSEA (<https://www.gsea-msigdb.org/gsea/index.jsp>), are accessible through publicly available links.

References

1. Cauley, J. A. The determinants of fracture in men. *J. Musculoskelet. Neuronal. Interact.* **2**, 220–221 (2002).
2. Melton, L. J., Chrischilles, E. A., Cooper, C., Lane, A. W. & Riggs, B. L. How many women have osteoporosis?. *J. Bone Miner. Res.* **20**, 886–892 (2005).
3. Van Geel, T. A., van Helden, S., Geusens, P. P., Winkens, B. & Dinant, G. J. Clinical subsequent fractures cluster in time after first fractures. *Ann. Rheum. Dis.* **68**, 99–102 (2009).
4. Riggs, B. Lawrence, Khosla, Sundeep & Melton III, L. Joseph. A Unitary Model for Involutional Osteoporosis: Estrogen Deficiency Causes Both Type I and Type II Osteoporosis in Postmenopausal Women and Contributes to Bone Loss in Aging Men. *J. Bone Miner. Res.* **13**, 763–773 (1998).
5. Raisz, L. G. Pathogenesis of osteoporosis: concepts, conflicts, and prospects. *J. Clin. Invest.* **115**, 3318–3325 (2005).
6. Khosla, Sundeep & Monroe, David G. Regulation of Bone Metabolism by Sex Steroids. *Cold Spring Harb. Perspect. Med.* **8**, a031211 (2018).

7. Adler, Robert A. et al. Managing Osteoporosis in Patients on Long-Term Bisphosphonate Treatment: Report of a Task Force of the American Society for Bone and Mineral Research. *J. Bone Miner. Res.* **31** 1, 16–35 (2016).
8. Levin, V. A., Jiang, X. & Kagan, R. Estrogen therapy for osteoporosis in the modern era. *Osteoporosis Int.* **29**, 1049–1055 (2018).
9. Gennari, L., Merlotti, D., Valleggi, F., Martini, G. & Nuti, R. Selective estrogen receptor modulators for postmenopausal osteoporosis: current state of development. *Drugs Aging* **24**, 361–379 (2007).
10. Cauley, J. A. et al. Effects of estrogen plus progestin on risk of fracture and bone mineral density: the Women's Health Initiative randomized trial. *JAMA-J. Am. Med. Assoc.* **290**, 1729–1738 (2003).
11. Nelson, E. R., Wardell, S. E. & McDonnell, D. P. The molecular mechanisms underlying the pharmacological actions of estrogens, SERMs and oxysterols: implications for the treatment and prevention of osteoporosis. *Bone* **53**, 42–50 (2013).
12. Canalis, E., Giustina, A. & Bilezikian, J. P. Mechanisms of anabolic therapies for osteoporosis. *N. Engl. J. Med.* **357**, 905–916 (2007).
13. Reid, I. R. Short-term and long-term effects of osteoporosis therapies. *Nat. Rev. Endocrinol.* **11**, 418–428 (2015).
14. Kawai, M., Modder, U. I., Khosla, S. & Rosen, C. J. Emerging therapeutic opportunities for skeletal restoration. *Nat. Rev. Drug Discov.* **10**, 141–156 (2011).
15. Coppe, J. P. et al. Senescence-Associated Secretory Phenotypes Reveal Cell-Nonautonomous Functions of Oncogenic RAS and the p53 Tumor Suppressor. *PLoS. Biol.* **6**, 2853–2868 (2008).
16. Coppe, J. P., Desprez, P. Y., Krtolica, A. & Campisi, J. The senescence-associated secretory phenotype: the dark side of tumor suppression. *Annu. Rev. Pathol.* **5**, 99–118 (2010).
17. Childs, B. G. et al. Senescent cells: an emerging target for diseases of ageing. *Nat. Rev. Drug Discov.* **16**, 718–735 (2017).
18. Baker, D. J. et al. Clearance of p16Ink4a-positive senescent cells delays ageing-associated disorders. *Nature* **479**, 232–236 (2011).
19. Rhinn, M., Ritschka, B. & Keyes, W. M. Cellular senescence in development, regeneration and disease. *Development* **146** (2019).
20. Sturmlechner, I., Durik, M., Sieben, C. J., Baker, D. J. & van Deursen, J. M. Cellular senescence in renal ageing and disease. *Nat. Rev. Nephrol.* **13**, 77–89 (2017).
21. Ambrosi, T. H. et al. Aged skeletal stem cells generate an inflammatory degenerative niche. *Nature* **597**, 256–262 (2021).
22. Farr, J. N. et al. Targeting cellular senescence prevents age-related bone loss in mice. *Nat. Med.* **23**, 1072–1079 (2017).
23. Xu, M. et al. JAK inhibition alleviates the cellular senescence-associated secretory phenotype and frailty in old age. *Proc. Natl. Acad. Sci. U. S. A.* **112**, E6301-6310 (2015).

24. Ferreira-Gonzalez, S. et al. Paracrine cellular senescence exacerbates biliary injury and impairs regeneration. *Nat. Commun.* **9**, 1020 (2018).
25. Barinda, A. J. et al. Publisher Correction: Endothelial progeria induces adipose tissue senescence and impairs insulin sensitivity through senescence associated secretory phenotype. *Nat. Commun.* **11**, 3837 (2020).
26. Almeida, M. et al. Skeletal involution by age-associated oxidative stress and its acceleration by loss of sex steroids. *J. Biol. Chem.* **282**, 27285–27297 (2007).
27. Sasaki, Y. et al. Estrogen-SIRT1 Axis Plays a Pivotal Role in Protecting Arteries Against Menopause-Induced Senescence and Atherosclerosis. *J. Atheroscler. Thromb.* **27**, 47–59 (2020).
28. Imanishi, Toshio, Hano, Takuzo & Nishio, Ichiro Estrogen reduces endothelial progenitor cell senescence through augmentation of telomerase activity. *J. Hypertens.* **23**, 1699–1706 (2005).
29. Palmer, A. K. et al. Targeting senescent cells alleviates obesity-induced metabolic dysfunction. *Aging Cell* **18**, e12950 (2019).
30. Advances in Marine Biology Novais, E. J. et al. Long-term treatment with senolytic drugs Dasatinib and Quercetin ameliorates age-dependent intervertebral disc degeneration in mice. *Nat. Commun.* **12**, 5213 (2021).
31. Zhu, Y. et al. The Achilles' heel of senescent cells: from transcriptome to senolytic drugs. *Aging Cell* **14**, 644–658 (2015).
32. Wang, Lichao et al. Targeting p21Cip1 highly expressing cells in adipose tissue alleviates insulin resistance in obesity. *Cell. Metab.* **34**, 75–89.e78 (2022).
33. Roos, C. M. et al. Chronic senolytic treatment alleviates established vasomotor dysfunction in aged or atherosclerotic mice. *Aging Cell* **15**, 973–977 (2016).
34. Hickson, LaTonya J. et al. Corrigendum to senolytics decrease senescent cells in humans: Preliminary report from a clinical trial of Dasatinib plus Quercetin in individuals with diabetic kidney disease. *EBioMedicine* **47**, 446–456 (2019).
35. Justice, J. N. et al. Senolytics in idiopathic pulmonary fibrosis: Results from a first-in-human, open-label, pilot study. *EBioMedicine* **40**, 554–563 (2019).
36. Martyanov, V., Whitfield, M. L. & Varga, J. Senescence Signature in Skin Biopsies From Systemic Sclerosis Patients Treated With Senolytic Therapy: Potential Predictor of Clinical Response? *Arthritis Rheumatol.* **71**, 1766–1767 (2019).
37. Hickson, L. J. et al. Senolytics decrease senescent cells in humans: Preliminary report from a clinical trial of Dasatinib plus Quercetin in individuals with diabetic kidney disease. *EBioMedicine* **47**, 446–456 (2019).
38. Yousefzadeh, M. J. et al. An aged immune system drives senescence and ageing of solid organs. *Nature* **594**, 100–105 (2021).
39. Ovadya, Y. et al. Impaired immune surveillance accelerates accumulation of senescent cells and aging. *Nat. Commun.* **9**, 5435 (2018).

40. Farr, J. N. et al. Independent Roles of Estrogen Deficiency and Cellular Senescence in the Pathogenesis of Osteoporosis: Evidence in Young Adult Mice and Older Humans. *J. Bone Miner. Res.* **34**, 1407–1418 (2019).
41. Shahnazari, M. et al. Differential maintenance of cortical and cancellous bone strength following discontinuation of bone-active agents. *J. Bone Miner. Res.* **26**, 569–581 (2011).
42. Josephson, A. M. et al. Age-related inflammation triggers skeletal stem/progenitor cell dysfunction. *Proc. Natl. Acad. Sci. U. S. A.* **116**, 6995–7004 (2019).
43. Deng, P. et al. Loss of KDM4B exacerbates bone-fat imbalance and mesenchymal stromal cell exhaustion in skeletal aging. *Cell Stem Cell* **28**, 1057–1073 e1057 (2021).
44. Zhou, Jun et al. Biomaterials and nanomedicine for bone regeneration: Progress and future prospects. *Exploration* **1**, 20210011 (2021).
45. Melton III, L. Joseph, Chrischilles, Elizabeth A., Cooper, Cyrus, Lane, Ann W. & Riggs, B. Lawrence. How Many Women Have Osteoporosis? *J. Bone Miner. Res.* **20**, 886–892 (2005).
46. Tang, W. et al. Bioinspired trimodal macro/micro/nano-porous scaffolds loading rhBMP-2 for complete regeneration of critical size bone defect. *Acta. Biomater.* **32**, 309–323 (2016).
47. Yue, R., Zhou, B. O., Shimada, I. S., Zhao, Z. & Morrison, S. J. Leptin Receptor Promotes Adipogenesis and Reduces Osteogenesis by Regulating Mesenchymal Stromal Cells in Adult Bone Marrow. *Cell Stem Cell* **18**, 782–796 (2016).
48. Manolagas, S. C. From estrogen-centric to aging and oxidative stress: a revised perspective of the pathogenesis of osteoporosis. *Endocr. Rev.* **31**, 266–300 (2010).
49. Chen, J. R. et al. Nox4 Expression Is Not Required for OVX-Induced Osteoblast Senescence and Bone Loss in Mice. *J. Bone Miner. Res.* **4**, e10376 (2020).
50. Geng, Q., Gao, H., Yang, R., Guo, K. & Miao, D. Pyrroloquinoline Quinone Prevents Estrogen Deficiency-Induced Osteoporosis by Inhibiting Oxidative Stress and Osteocyte Senescence. *Int. J. Biol. Sci.* **15**, 58–68 (2019).
51. Jeon, O. H. et al. Local clearance of senescent cells attenuates the development of post-traumatic osteoarthritis and creates a pro-regenerative environment. *Nat. Med.* **23**, 775–781 (2017).
52. Sun, Lili et al. Recapitulation of In Situ Endochondral Ossification Using an Injectable Hypoxia-Mimetic Hydrogel. *Adv. Funct. Mater.* **31**, 2101589 (2020).
53. Minoru, K. et al. KEGG for linking genomes to life and the environment. *J. Nucleic Acids.* **36**, 480–484 (2008).
54. Luo, W., Pant, G., Bhavnasi, Y. K., Blanchard, S. G., Jr. & Brouwer, C. Pathview Web: user friendly pathway visualization and data integration. *Nucleic Acids Res.* **45**, W501-W508 (2017).
55. Mootha, Vamsi K. et al. PGC-1 α -responsive genes involved in oxidative phosphorylation are coordinately downregulated in human diabetes. *Nature Genet.* **34**, 267–273 (2003).

Figures

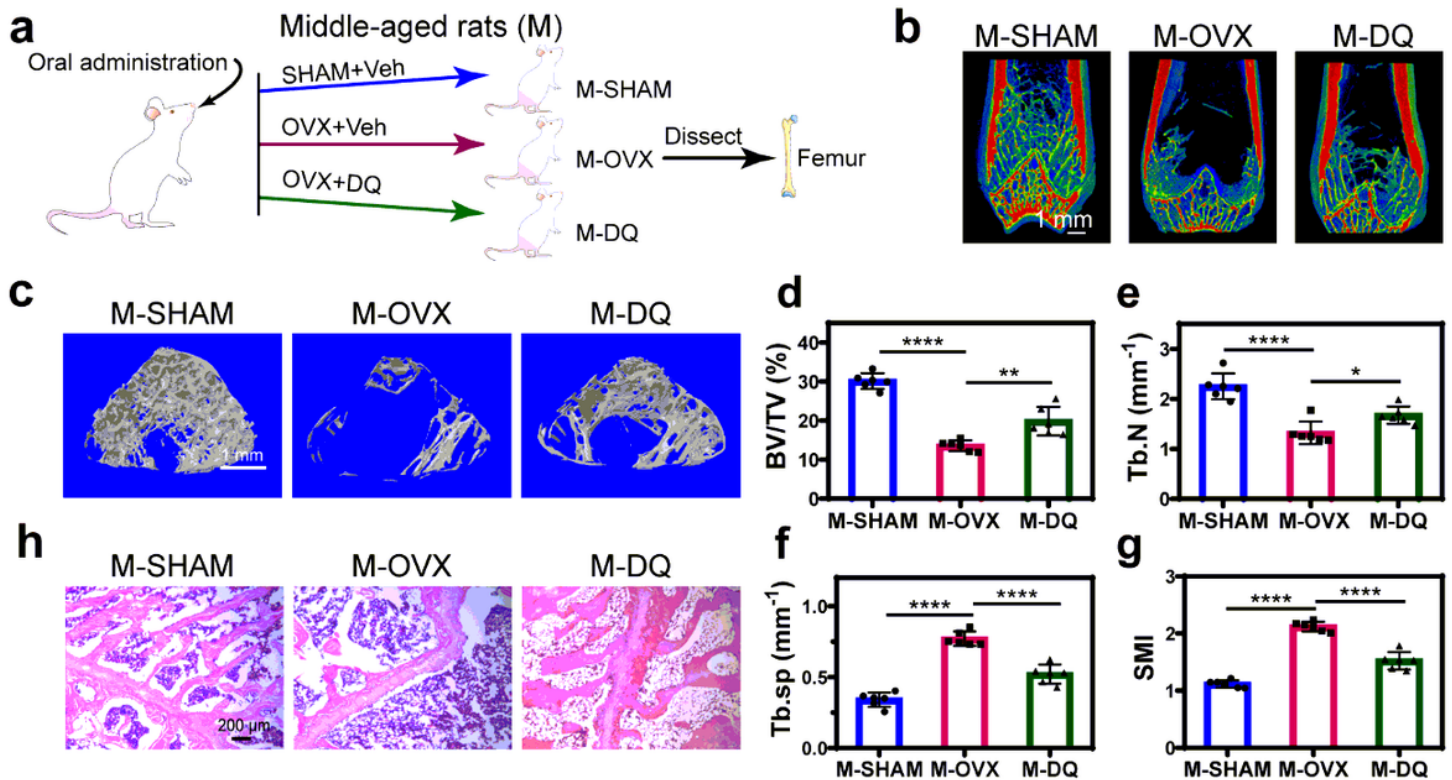


Figure 1

Systematic treatment of senolytic drug DQ prevented bone loss in middle-aged postmenopausal osteoporotic rats (PMO rats). (a) Experimental design for testing DQ treatment effect on PMO. (b) Representative micro-CT (μCT) 2D images of femur from middle-aged SHAM (M-SHAM), OVX (M-OVX) and DQ-treated (M-DQ) groups; scale bar is 1 mm. (c) Representative μCT 3D images of areas in distal femur; scale bar is 1 mm. Quantification of μCT-derived (d) bone volume fraction (BV/TV; %), (e) trabecular number (Tb.N; mm⁻¹), (f) trabecular separation (Tb.Sp; mm), and (g) structure model index (SMI). (h) Representative hematoxylin-eosin staining (H&E) staining images of femurs; scale bar is 200 μm. Data are represented as mean ± s.e.m. *p<0.05, **p < 0.01, ***p < 0.001, as determined by one-way ANOVA analyses with Tukey's post-hoc test.

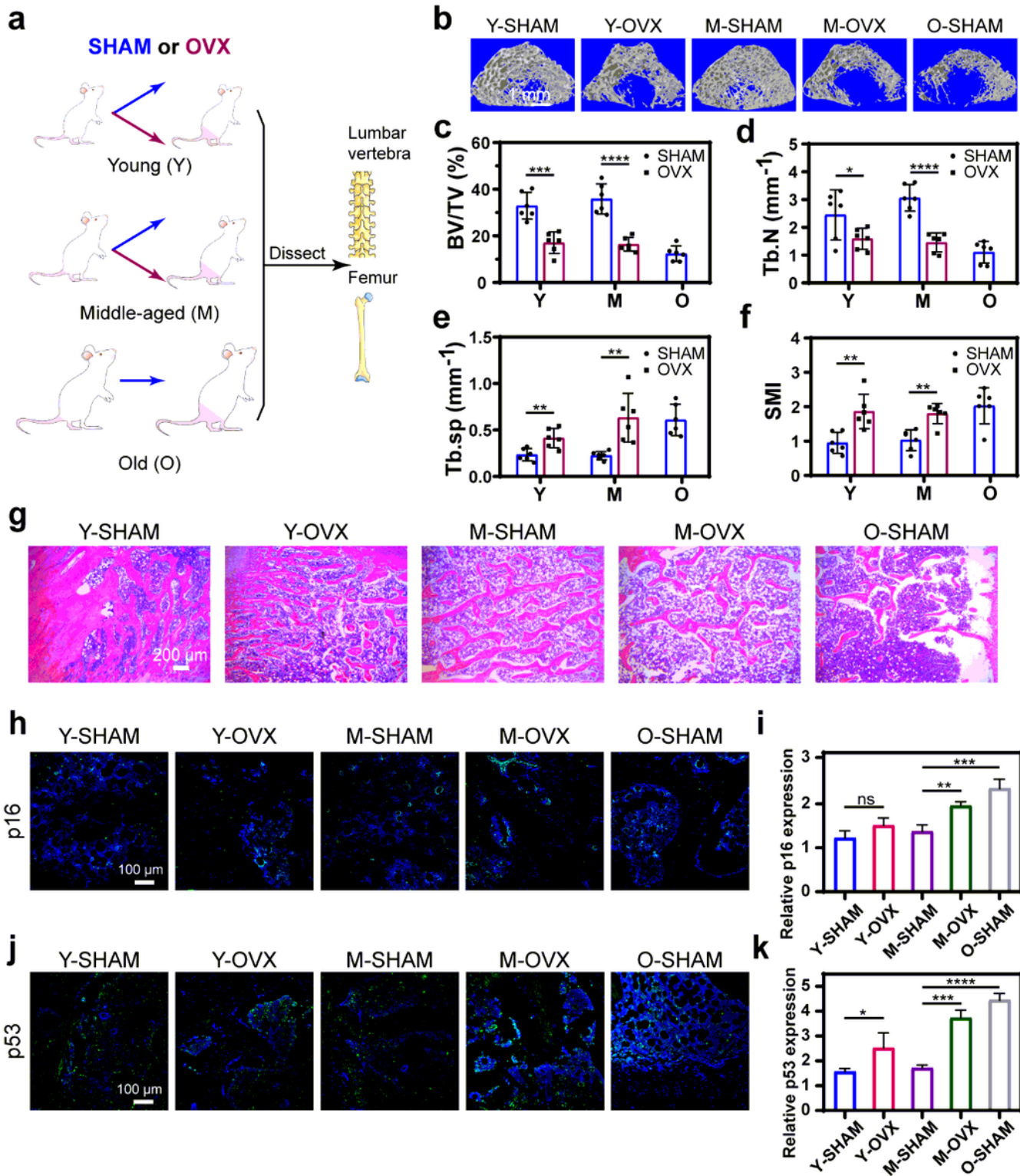


Figure 2

Accumulation of SnCs accelerated bone loss in middle-aged PMO rats. (a) Experimental design for testing whether SnCs contributed to PMO; young and middle-aged rats were SHAM (Y-SHAM or M-SHAM) or OVX (Y-OVX or M-OVX) operated, with old SHAM-operated (O-SHAM) rats as natural aging comparison. (b) Micro-CT (μ CT) 3D images of femur; scale bar is 1 mm. Quantification of μ CT-derived (c) bone volume fraction (BV/TV; %), (d) trabecular number (Tb.N; mm⁻¹), (e) trabecular separation (Tb.Sp; mm) and (f)

structure model index (SMI). (g) Optical photographs for hematoxylin-eosin staining (H&E) staining in different groups; scale bar is 200 μ m. (h, i) Immunofluorescent image and quantification of p16 expression. Sections were co-stained for p16 (green) and nuclei (blue). (j, k) Immunofluorescent image and quantification of p53 expression. Sections were co-stained for p53 (green) and nuclei (blue). Data are represented as mean \pm s.e.m. * $p < 0.05$, ** $p < 0.01$, *** $p < 0.001$, **** $p < 0.0001$, ns, not significant, as determined by one-way ANOVA analyses with Tukey's post-hoc test for all comparisons.

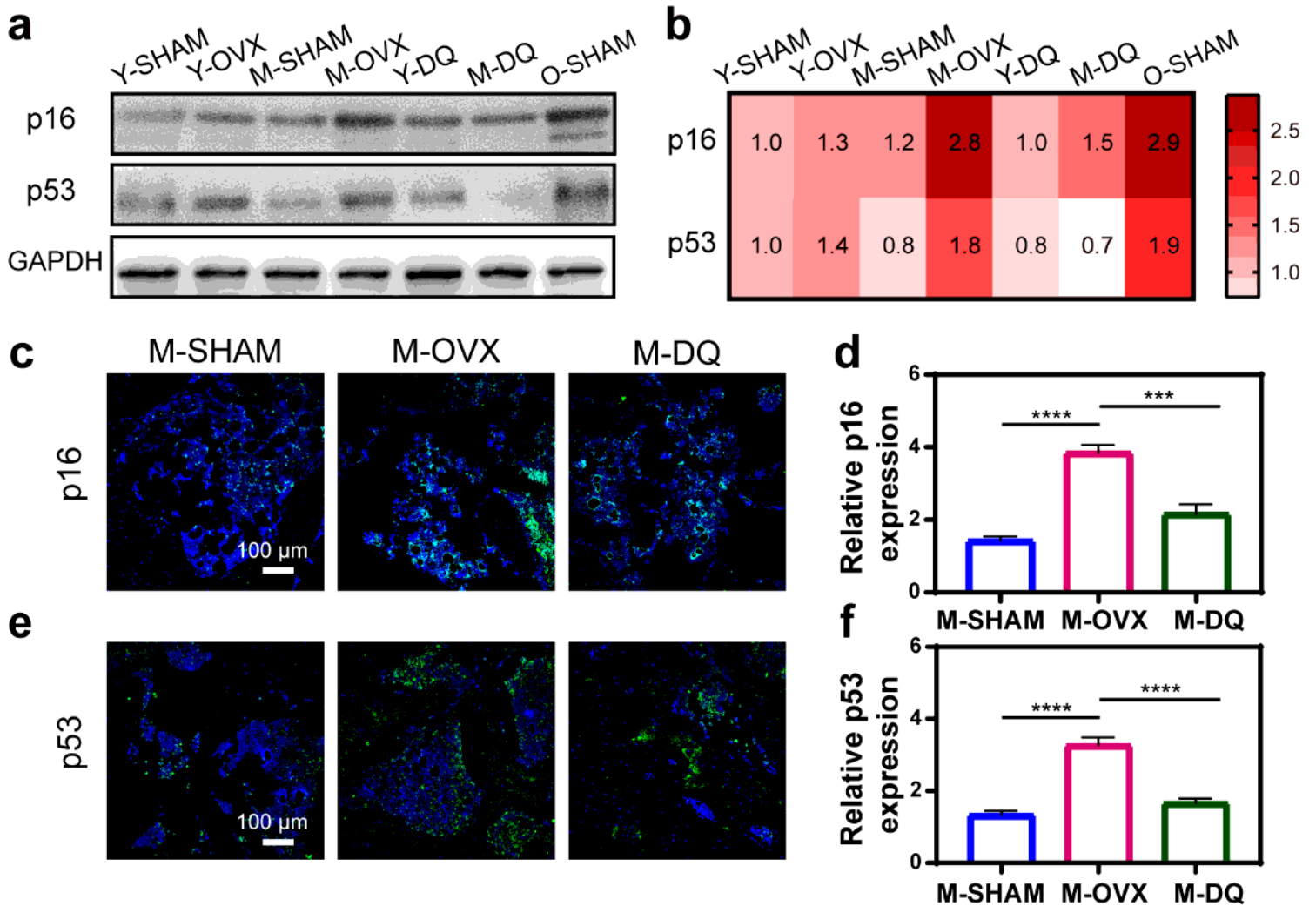


Figure 3

DQ eliminated SnCs in middle-aged PMO rats. (a) P16 and p53 expression of lumbar vertebra analyzed by western blot. (b) Quantification of western blot analysis. (c, d) Immunofluorescent images and quantification of p16 expression in femur; scale bar is 100 μ m. (e, f) Immunofluorescent images and quantification of p53 expression in femur; scale bar is 100 μ m. Data are represented as mean \pm s.e.m. *** $p < 0.001$, **** $p < 0.0001$, as determined by one-way ANOVA analyses with Tukey's post-hoc test for all comparisons.

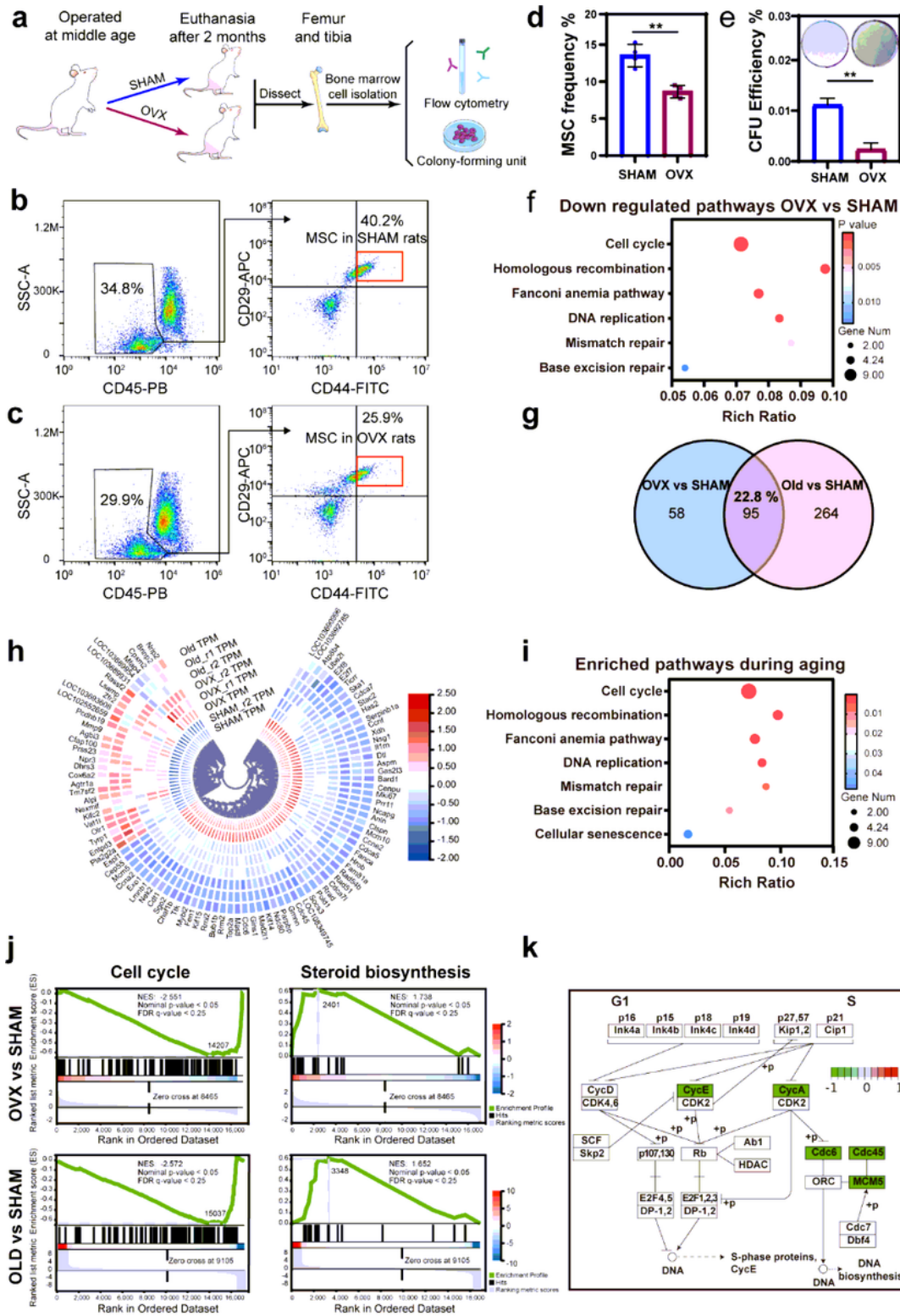


Figure 4

MSCs exhibited senescence-associated characteristics in middle-aged PMO rats. **(a)** Experimental flowchart for identification and self-renewal capacity evaluation of MSCs obtained from middle-aged SHAM and middle-aged OVX rats. The femur and tibia were dissected after 2 months of operation. **(b, c)** Flow cytometry analysis with gating scheme for identification of MSCs based on the expression of CD45, CD44 and CD29. **(d)** Summary plot of MSC frequency from cytometry. **(e)** Colony-forming unit (CFU)

assay of cells isolated from SHAM or OVX bone marrow. **(f)** Representative KEGG pathways of downregulated genes from OVX vs. SHAM ($p \leq 0.05$, $|\log \text{fold change}| \geq 1$). **(g)** Venn diagrams showing differentially expressed genes (DEGs) of MSCs from OVX vs. SHAM and Old vs. SHAM (OVX and Old; SHAM). **(h)** Heat map representing gene-expression values of the 95 genes in the intersection of OVX vs. SHAM and Old vs. SHAM. **(i)** Representative KEGG pathways of DEGs from intersection of OVX vs. SHAM and Old vs. SHAM. **(j)** GSEA plots of MSCs from OVX vs. SHAM and Old vs. SHAM ($|\text{NES}| > 1$, Nominal p-value < 0.05 , FDR < 0.25). **(k)** Schematic summarizing the DEGs from OVX vs. SHAM related to cell cycle regulation during G1 to S transition using KEGG clustering pathway analysis.

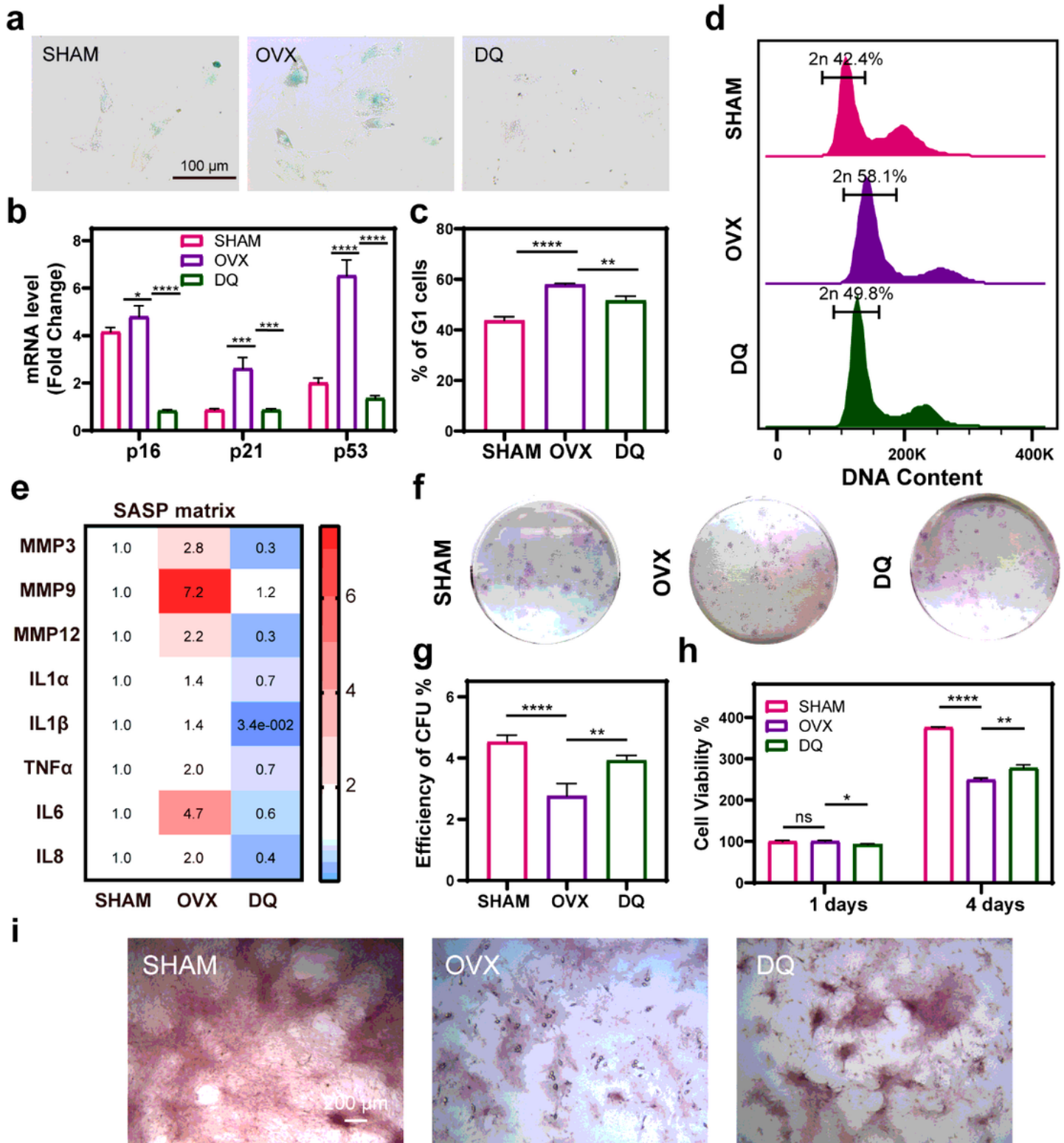


Figure 5

DQ rescued MSC exhaustion and restored MSC function via attenuating SASP. (a) Senescence-associated- β -galactosidase (SA- β -gal) staining of MSCs cultured in conditioned culture medium (CM) for 7 days which consisted of serum collected from different rats: M-SHAM (SHAM), M-OVX (OVX), and M-DQ rats treated (DQ); the scale bar is 100 μ m. (b) RT-qPCR analysis of mRNA expression changes of the senescence effectors, p16Ink4a (p16), p21Cip1 (p21), and p53 (p53), in MSCs treated with different CM.

(c) Summary plot of G1 cell cycle inhibited MSCs. (d) Cell cycle analysis of MSCs as a typical character of senescence. (e) RT-qPCR analysis of SASP factors in MSCs treated for 7 days indicating estrogen deficiency accelerated MSCs senescence and dysfunction via SASP. (f) CFU assay of MSCs treated with CM. (g) Quantification of CFU assay. (h) Cell viability of MSCs treated with CM for 1 day and 4 days. (i) *In vitro* Alizarin red S (ARS) staining images in osteogenic differentiation conditioned medium; scale bar is 200 μ m. Data are represented as mean \pm s.e.m. * $p < 0.05$, ** $p < 0.01$, *** $p < 0.001$, **** $p < 0.0001$, ns, not significant, as determined by one-way ANOVA analyses with Tukey's post-hoc test for all comparisons.

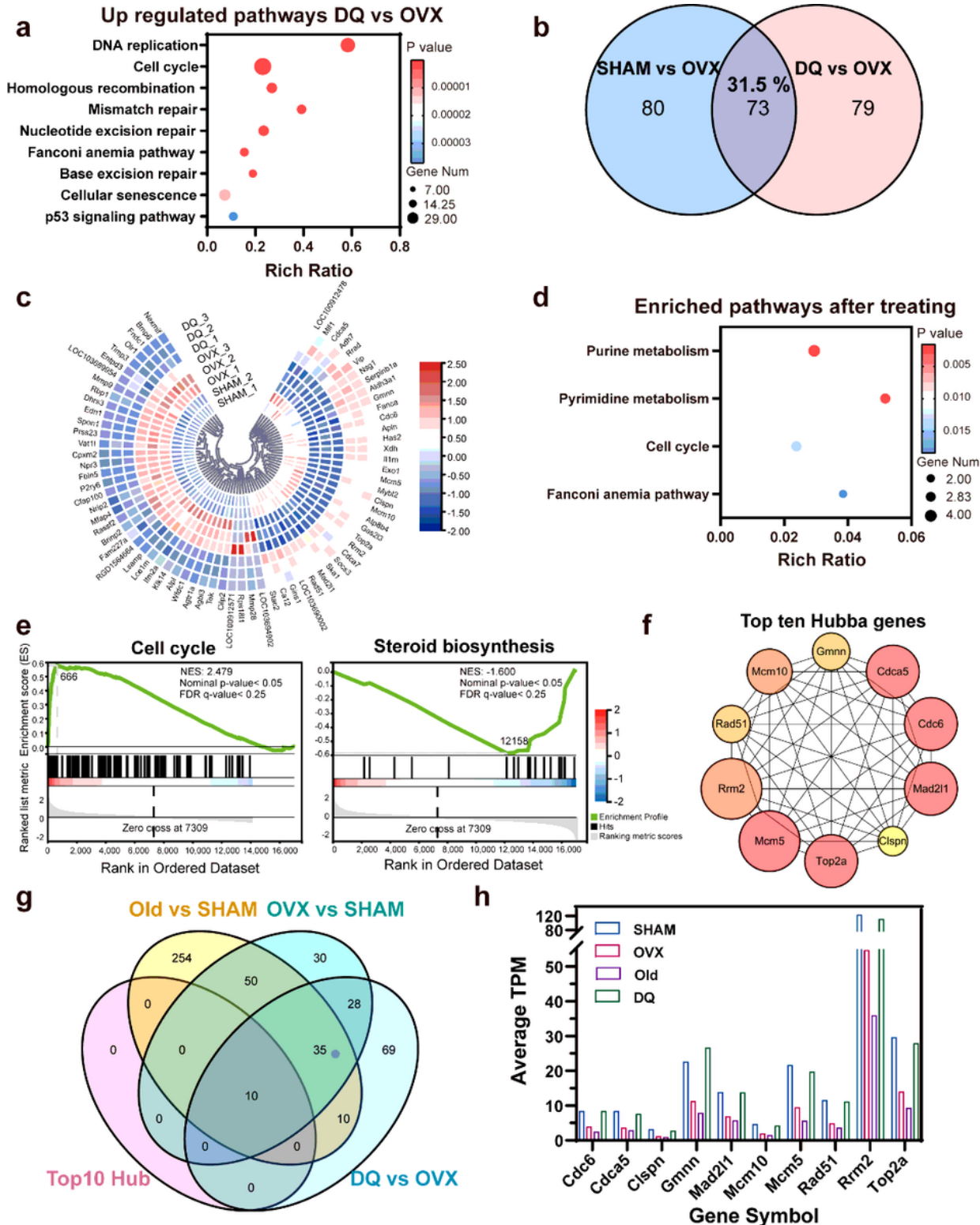


Figure 6

DQ treatment attenuated transcriptomic regulation of senescence-associated pathways modulated in MSCs. (a) Representative KEGG pathways of upregulated genes from DQ vs. OVX (p value ≤ 0.05 , $|\log$ fold change ≥ 0.585). (b) Venn diagrams show DEGs in MSCs from SHAM vs. OVX and DQ vs. OVX. (c) Heat map representing gene-expression values of the 73 genes in the intersection of SHAM vs. OVX and DQ vs. OVX. Hierarchical clustering of these genes reveals that MSCs cultured in DQ CM cluster with that in SHAM CM. (d) Representative KEGG pathways of DEGs from intersection of SHAM vs. OVX and DQ vs. OVX. (e) GSEA plots demonstrate that DQ treated MSCs correlate with gene sets for cell cycle steroid biosynthesis in a opposite way to OVX MSCs, but in a similar way to SHAM MSCs ($|\text{NES}| > 1$, Nominal p -value < 0.05 , FDR < 0.25). (f) Top ten hub genes involved in the protein-protein interaction (PPI) network are predicted using KEGG clustering pathway analysis of DEGs of DQ vs. OVX, indicating the promising key genes after DQ treatment. (g) Venn diagrams show the top ten hub genes of DQ vs. OVX are all in the intersection of OVX vs. SHAM, Old vs. SHAM and DQ vs. OVX. (h) Gene expression in MSCs treated with four different CMs show the consistent expression change of the top ten hub genes.

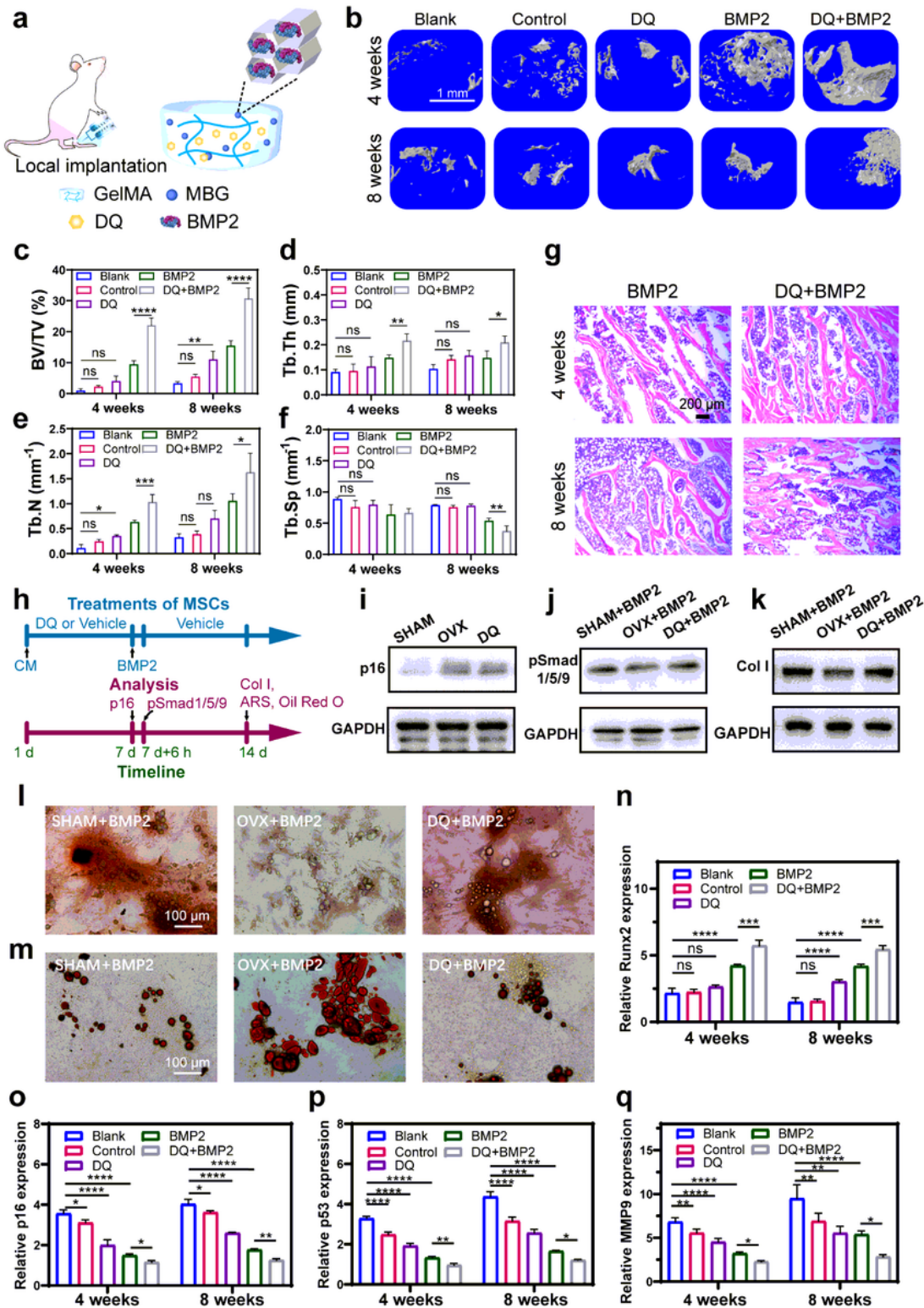


Figure 7

Local implantation of DQ-encapsulated and BMP2-fixed hydrogel rejuvenated bone regeneration. (a) Schematic fabrication of injectable gelatin methacryloyl hydrogel (GelMA) and bioglass microsphere with mesoporous pores (MBG) to realize DQ and BMP2 release in a sequential way. (b) Micro-CT reconstructions of calluses at week 4 and week 8 after fracture; scale bar is 1 mm. Quantification of μ CT-derived (c) bone volume fraction (BV/TV; %), (d) trabecular thickness (Tb.Th; mm), (e) trabecular number

(Tb.N; mm-1) , (f) trabecular separation (Tb.Sp; mm). (g) H&E staining images of newly formed bone. (h) Scheme of treatments and analysis at specific time points. (i) Expression of p16 protein after being cultured in CM for 7 days. (j) Expression of pSmad1/5/9 protein after being cultured in CM for 7 days and administrated with BMP2 for another 6 hours. (k) Expression of Col protein after being cultured in CM for 7 days and then BMP2 dissolved in different CM for another 7 days in chronological order. (l) ARS staining of MSCs at day 14. (m) Oil red staining of MSCs at day 14. (n) Quantification of Runt-Related Transcription Factor 2 (Runx2) expression by immunofluorescent staining. (o) Quantification of p16 expression by immunofluorescent staining. (p) Quantification of p53 expression by immunofluorescent staining. (q) Quantification of Matrix Metalloproteinase 9 (MMP9) expression by immunofluorescent staining. * $p < 0.05$, ** $p < 0.01$, *** $p < 0.001$, **** $p < 0.0001$, ns, not significant, as determined by one-way ANOVA.

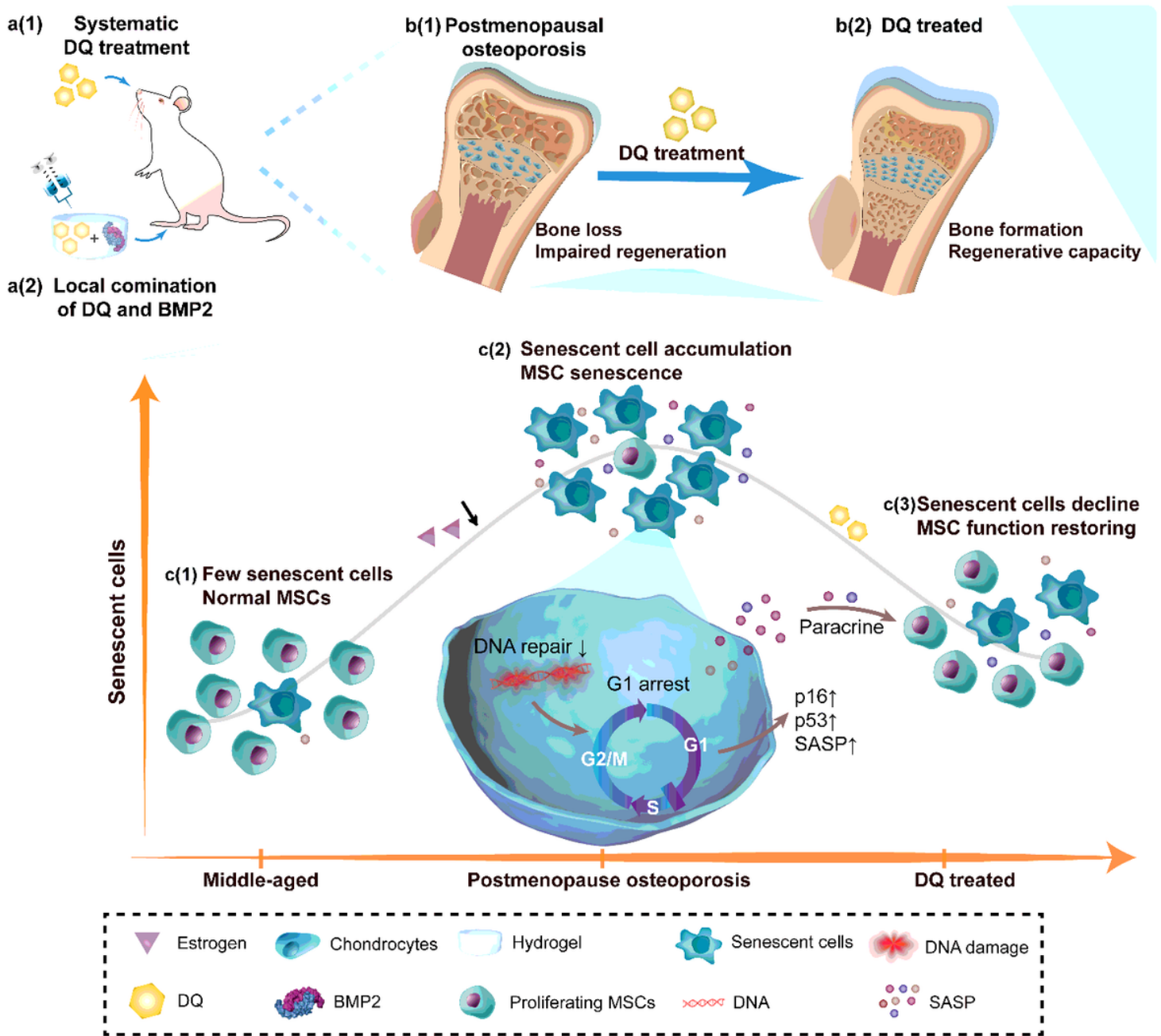


Figure 8

Graphical abstract of DQ systematically ameliorated PMO and locally rejuvenated PMO related bone regeneration. PMO and related diseases are relevant to SnCs accumulation and MSC senescence in middle-aged rats. Senolytic drug DQ ameliorated PMO and related diseases, as proved by systematically preventing bone loss and locally rejuvenating bone regeneration, in synergy with BMP2. Mechanistically, MSCs in PMO exhibited senescent-associated characters, including damaged DNA repair, G1 arrest, exhaustion and dysfunction. DQ diminished SnCs, rescued MSC exhaustion and recovered MSC function by attenuating SASP secretion.

Supplementary Files

This is a list of supplementary files associated with this preprint. Click to download.

- [2.Supplementaryfiles.docx](#)
- [3.SupplementaryfilesTableS3.xlsx](#)
- [3.SupplementaryfilesTableS4.xlsx](#)
- [3.SupplementaryfilesTableS5.xlsx](#)